ARMA 18–318

Pore characterization of mine shales by low pressure nitrogen adsorption and mercury intrusion porosimetry: Implication on water retention behavior of shales

Guijie Sang, Shimin Liu *, Rui Zhang, Derek Elsworth

Department of Energy and Mineral Engineering, G3 Center and Energy Institute, Pennsylvania State University, University Park, PA 16802, USA

ABSTRACT: The moisture-induced shale deterioration is considered one of the primary roof stability issues in underground coal mines. Understanding of the pore morphology of shale will provide clues to its water retention behavior and strength degradation due to seasonal changes in humidity in coal mines. In this study, low pressure nitrogen adsorption and high pressure mercury intrusion porosimetry were employed to characterize pore structure of one fireclay and four coal mine shales. The results suggest that the porosity and specific surface area (SSA) for all five samples are dominated by mesopores (2-50 nm). Based on the obtained pore size distributions, water retention curves are built and are closely associated to water adsorption behavior. Due to the dominant mesopores, the studied fireclay and shales behave a strong water retention capacity with matric suction reaching ~ 100-150 MPa at degree of saturation equals ~3%. Larger porosity and/or SSA tend to have higher water adsorption. Despite a relatively low porosity of the fireclay, the large matric suction over the whole range of degree of saturation corresponding to the high proportion of micro/meso-pores lead to a strong water retention capacity, which in turn contributes to water adsorption.

1. INTRODUCTION

It was reported to Mine Safety and Health Administration (MSHA) by about 800 coal mines that nearly 11,600 non-injury roof falls occurred in active coal mining areas from 1999 to 2008 [1]. Though causing no direct fatality or injury to miners, massive non-injury roof falls over time can disrupt regular mining activity, impair ventilation systems, impede passages of miners, extend to the anchorage zone of roof bolts, and cause some potential ground control problems [2]. Most roof fall incidents are associated to several contributory factors such as slip in the roof, laminated roof, draw rock, wet roof, rider seam, clay veins and cutter failure [1–5]. All of these factors are linked more or less with the weathering behavior of roof shales and their moisture sensitivity. Despite great strides in the design of support systems, deterioration of roof rocks continues to occur due to seasonal changes in humidity and temperature in underground coal mines [6,7].

Shale deterioration is strongly related to rock porosity and pore structure in relation to thermodynamic properties of water present in shale pores. In general, shales with higher porosity and specific surface area (SSA) tend to have higher capacity to water adsorption, while a large amount of water adsorption or wetting/drying cycle could be the main cause of strength degradation and shale deterioration [8]. Previous study [9] attributes shale swelling, slaking and weakening to the release of capillary suction between grains, which is tightly related to pore size distribution (PSD). Another study on water-softening property of siltstone indicates that the reduction of rock strength in presence of moisture is mainly attributed to the changes of the microstructure and material composition [10]. Therefore, pore structure characterization contributes to the understanding of moisture induced strength reduction of coal mine shales and lays a foundation for roof support design and ground control management. Besides, for porous rocks, porosity, SSA, fractal character and PSD are very important aspects of pore characteristics influencing capillary pressure [9], water sorptivity [11], connectivity [12], permeability [13,14], stress transition [15], fluid storage and transportation [16,17], and fracture initiation [18], etc. These mechanisms governed by pore structures can hardly be specified by a macroscopic presentation of rock samples. Characterization of pore structure of rocks may become a good way to specify these microscopic mechanisms and therefore, to connect the gap between physical and/or mechanical performance of rocks and their pore characteristics.

In a prior work, various techniques has been applied to characterize pore structure of shale matrix such as atomic

force microscopy (AFM) [19], field emission scanning electron microscopy (FE-SEM) [20,21], high pressure mercury intrusion porosimetry (MIP) and low-pressure gas adsorption [22,23], ultra-/small angle neutron scattering (USANS/SANS) [24–26]. Shales have a much more complex pore system than coal and conventional reservoir rocks such as sandstone and limestone, since shales combine conventional coarse porosity from inorganic minerals such as quartz or carbonates and ultrafine porosity from both organic matter (kerogen) and clay minerals. The study of Cretaceous shale using USANS/SANS [24] and Northwestern Hunan shale using FE-SEM, MIP and gas adsorption [22] show that meso- and micropores contributes dominantly to the total porosity and specific surface area. The combination of nitrogen adsorption technique and mercury porosimetry technique shows that the dominance of illite-smectite clays can contribute to the presence of micropores and fine mesopores in shales [23], since illite-smectite clays presents a multiscale pores which are associated with spaces between clay platelet bundles (10-100 nm), interlayer spaces (<10 nm) and spaces between aggregates (>10 μm) [23,27,28].

In this study, we investigate the pore characteristics of one fireclay and four shale samples from Illinois coal mines using a combination of low-pressure N_2 adsorption and MIP techniques. The porosity, SSA, as well as PSDs obtained by the two techniques are discussed for the studied five samples. Besides, linkage between pore size distributions of the five samples and their water retention characteristics is also built to discuss water retention and adsorption behavior.

2. PORE STRUCTURE CHARACTERIZATION

2.1 Sample collection and mineralogical compositions

A total of five samples were collected from two Illinois coal mines - Bear Run Mine located at Carlisle, Indiana, and Wildcat Hills Mine located at Equality, Illinois. The samples were collected from actively mined areas, which were not weathered since being mined and well preserved at a proper temperature and humidity condition. The description of the samples is shown in Table 1. The two gray shales (6R and 5A) and the fireclay (7F) contain negligible TOC compared to the two black shales - 6F and H6, which contain ~31.4% and ~21.4% TOC, respectively.

The weight percentage of mineralogical composition based on X-ray diffraction analysis together with TOC content for the five samples are shown in Figure 1. Overall, the five samples show a broad range of inorganic fraction compositions. The dominant minerals for the studied five samples are quartz, clays (mainly illite), mica (muscovite) and other phyllosilicate minerals including chlorite, clinochlore, dickite, halloysite, and palygorskite. Specifically, 7F fireclay contains 40.6% quartz and 59.4% clays, mica and other phyllosilicate minerals while contains no pyrite, albite and carbonates. The two gray shales (6R and 5A) contain no pyrite and carbonates while contain 2.7% and 3.4% albite. The two black shales (6F and H6) contain 2.7% and 3.1% pyrite respectively. 6F black shale contains 1.4% calcite and H6 black shale contains 3.3% dolomite. Besides, H6 black shale contains 8.6% montmorillonite and the highest content of illite (29.3%) compared to the other four samples. All the five samples contain relatively high clay minerals, which may be the root cause of weak roof characters in underground coal mines due to the hydrophilic character of clay minerals.

Table 1. Description of the samples from Illinois basin in Pennsylvanian age.

sample	shale type	mine name	location	coal seam
7F	fireclay	Bear Run Mine	Carlisle, Indiana	Danville (No.7)
6R	gray shale	Bear Run Mine		Hymera (No.6)
5A	gray shale	Bear Run Mine		Springfield (No.5A)
6F	black shale	Bear Run Mine		Hymera (No.6)
H6	black shale	Wildcat Hills Mine	Equality, Illinois	Herrin No.6

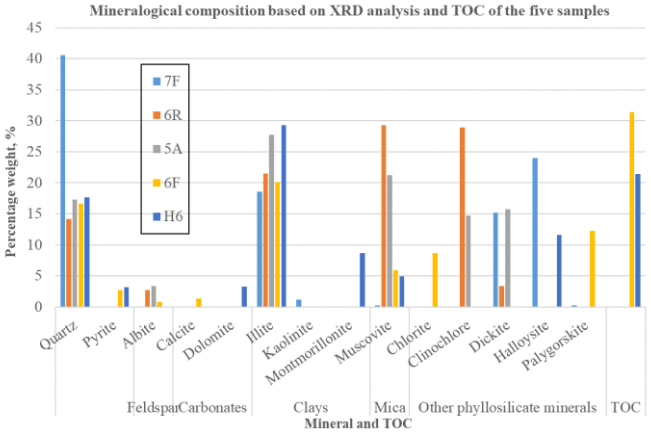

Figure 1. Mineralogical composition of the studied five samples based on XRD analysis together with TOC.

2.2. Low pressure N_2 adsorption analysis

N_2 ad/de-sorption isotherms were collected at 77 K using a Micromeritics ASAP 2020 apparatus loacated at Penn State University on 60-80 mesh powder samples. To avoid damaging TOC and ensure the completion of degassing process, the five samples including the two organic-rich shales (6F and H6) were degassed at ~80 °C under vacuum for approximately 16 hours prior to the nitrogen adsorption experiments. The adsorption isotherms were obtained under a wide range of relative pressure from 0.009 to 0.994. The obtained isotherms

were intepreted using Brunauer-Emmett-Teller (BET) model and density functional theory (DFT) model for the estimation of the surface area and total pore volume. Pore size distributions for the measured five samples were obtained using DFT model. Details on the interpretion of the N_2 sorption isotherms were discussed in previous study [29].

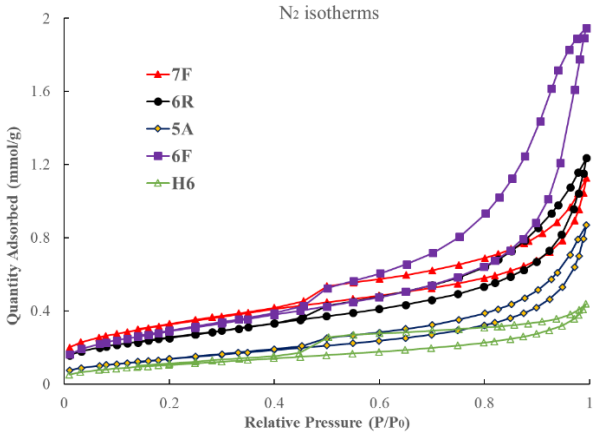

Figure 2. Low-pressure nitrogen adsorption isotherms for the studied five samples at liquid nitrogen temperature (77K).

Low-pressure nitrigen ad/de-sorption isotherms at 77 K along with hysteresis patterns can be used to investigate the physisorption mechanisms and characterize pore structure in the large micropore to macropore range. The ad/de-sorption isotherms for the five samples are shown in Figure 2. According to the IUPAC classification, all the samples show a H3 type of hysteresis loop which is indicative of the process of capillary condensation and evaporation within the mesopores, suggesting that the shale samples dominantly contain slit-shaped pores [29]. Micropores in certain clay minerals may be associated with slit-shaped pores [23,30]. Another observation on the hysteretic patterns of the studied five samples is the sudden closure of the desorption branch at p/p_0 around 0.45-0.5, called 'Tensile Strength Effect' [31]. This is attributed to the collapse of the hemispherical meniscus during capillary evaporation in pores with a size of approximately 4 nm. This causes that the lower limit of the pore size evaluated from the desorption brach is ~4-5 nm. Therefore, instead of desorption branch, the adsorption branch is applied based on DFT theory for pore size calculations in this work.

Nitrogen adsorption results are listed in Table 2. 7F fireclay presents the highest BET surface area (26.23 m^2/g). For the two black shales, 6F black shale has a relatively higher surface area (23.67 m^2/g) while H6 sample presents the least (8.88 m^2/g). Combining with the bulk density obtained by MIP which will be presented in the next section, the N_2 porosity (the product of total pore volume and bulk density) can be estimated and is shown in Table 2. 6F black shale presents the highest porosity (7.8%) and H6 the least (2.5%), with the average porosity of all the samples being 5.1%.

Table 2. Nitrogen adsorption results.

sample	BET SSA, m^2/g	total pore volume [a], cm^3/g	total SA[a], m^2/g	porosity [b], %
7F	26.23	0.0201	10.15	5.0
6R	20.64	0.0254	9.37	6.3
5A	11.49	0.0154	6.43	3.8
6F	23.67	0.0488	12.48	8.2
H6	8.88	0.0139	3.86	2.5

a. Results are based on DFT theory. SA represents surface area.
b. Porosity is calculated using bulk density obtained by MIP.

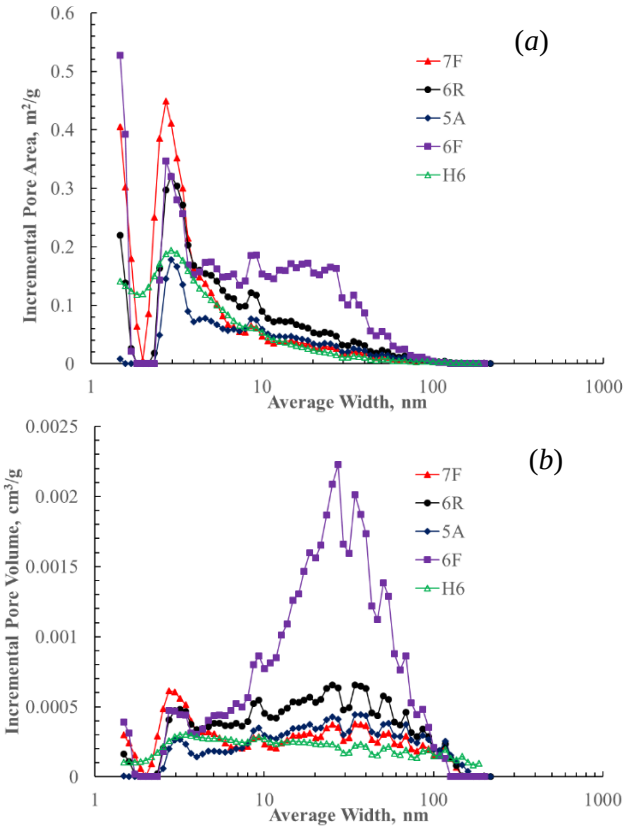

Figure 3. Distributions of pore surface area (*a*) and volume (*b*) for the studied five samples.

Pore size distribution can be presented as cumulative, incremental, or differential distribution curves [23,25,28]. The incremental volme and area with respect to pore width for the studied samples (Figure 3) were obtained based on DFT method, which shows a bimodal distribution of surface area (peaks at ~3 nm and ~9 nm) and pore volume (peaks at ~3 nm and ~25 nm). 6F black shale presents obviously larger surface area and volume for pores between 10 nm and 100 nm than other samples. Contribution of larger micropores (1.5-2 nm), mesopores (2-50 nm) and macropores (50-200 nm) to total pore surface area and total pore volume for the studied five samples are shown in Figure 4. Mesopores with the size

between 2-50 nm contribute predominantly to the total pore surface area (80%-96%) and toal pore volume (65%-82%). Large micorpores (1.5-2 nm) for 7F fireclay, 6R gray shale, 6F and H6 black shales account for ~8%-18% total pore surface area and ~5%-22% total pore volume. Large micorpores (1.5-2 nm) for 5A gray shale account for negligible total pore surface area and 3% total pore volume. Since the probe size of N_2 sorption based on DFT theory is limited to ~1.5 nm, smaller micropores (<1.5 nm) were not taken into consideration.

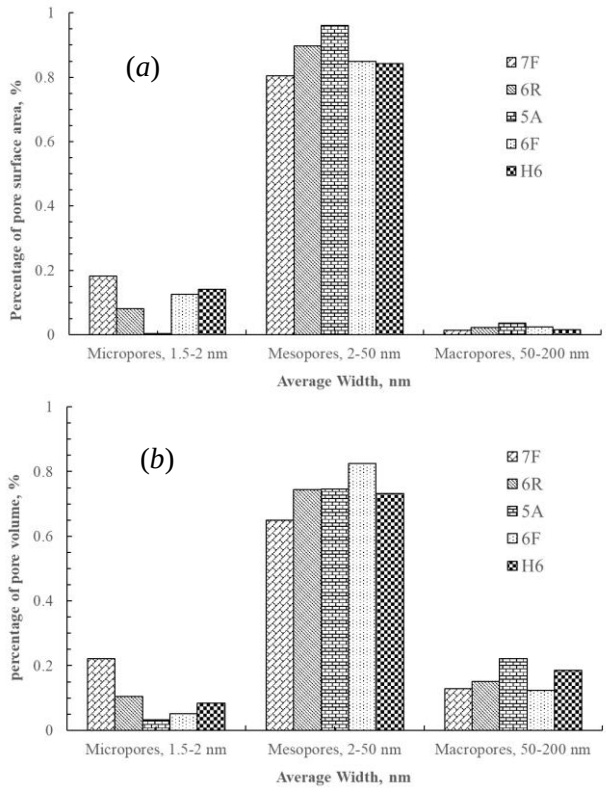

Figure 4. Percentage of surface area (*a*) and volume (*b*) of measured micropore, mesopores, and macropores for the studied five samples.

2.3. Mercury intrusion porosimetry analysis

The total porosities, SSAs and PSDs of the studied five samples were also obtained based on mercury porosimeter analysis using a Micrometrics Autopores V 9620 located in MCL at Penn State University at pressures up to 60,000 psia. Different from powder samples used for low pressure nitrogen adsorptoin, small bulk pieces with the dimension approximately 0.5-1 cm were prepared to fit into a 12 cc penetrometer for the MIP test. Total pore volume, SSA and distribution of pore size ranging from 3 nm to tens of microns were generated from the pressure versus intrusion/extrusion volume data using the Washburn equation [32].

Being a stongly non-wetting fluid (high contact angle), mercury does not penatrate into pores spontaneously by capillary action. Through an external pressure, mercury is forced to intrude pores with specifc sizes determined by the Washburn equation [32]. The amount of pressure required for mercury intrusion is inversely proportional to the size of the pores. Besides, assuming that pores are in cylindrical shape, mercury intrusion analysis only quantitatively detects pore throat, the entrance toward a pore, rather than actal inner pores [33]. The intrusion and extrusion curves of the studied five samples are shown in Figure 5. 6F black shale presents the highest quantity of mercury intrusion at the high pressure up to ~6000 psia, suggesting the largest cumulative pore volume for pores larger than ~3 nm, while H6 black shale presents the lowest cumulative pore volume (> ~3 nm). The 7F fireclay and the two gray shales (6R and 5A) have the similar quantity of intrusion. This is consistent with the low pressure nitrogen adsorption as is described in the former section.

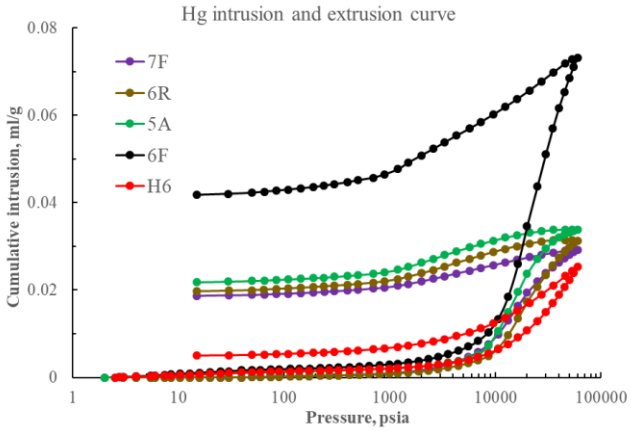

Figure 5. Mercury intrusion and extrsion curves showing hysteresis phenomena.

Besides, an obvious hysteresis occurs between mercury intrusion and extrusion process (Figure 5). There are two main explainations for this. First, it may arise due to change in contact angle for intruding and extruding menisci [34,35]. However, Conner et al. [36] stated that thermodynamic arguments for contact-angle hysteresis are hard to justify and are inadequate to explain many of the phenomena in porosimetry. Instead, structural hysteresis is expected to occur where the pressures for intrusion and extrusion processes are controlled by different aspects of the pore structure. For example, for 'ink-bottle' pores consisting of large pore bodies interspersed with narrow pore necks, intrusion is controlled by pore neck sizes, wheras extrsion is controlled by pore body sizes [36,37]. Later on, Conner et al. [38] compared PSDs of compressed aerosols measured by both mercury porosimtry and nitrogen adsorption, concluding that mercury intrusion corresponds to nitrogen desorption, characterizing the constrictions within the void network (pore throats), while mercury extrusion corresponds to nitrogen adsoption, characterizing the openings within the void network (pore body). PSDs of the studied five samples by mercury intrusion and extrusion data are shown in Figure 6. The volume-distribution curves were presented by taking the

derivative of the volume intruded (or extruded) with respect to the diatmeter of intrusion (or extrusion). The overall trends of the PSDs for the studied five samples are same. Difference in PSDs of the studied five samples obtained from intrusion and extrusion process can be due to structural hysteresis. From Figure 6, despite the limitation in detecting micropores (<2 nm), mercury intrusion/extrusion is applicable over a wide range of pore sizes up to tens of microns.

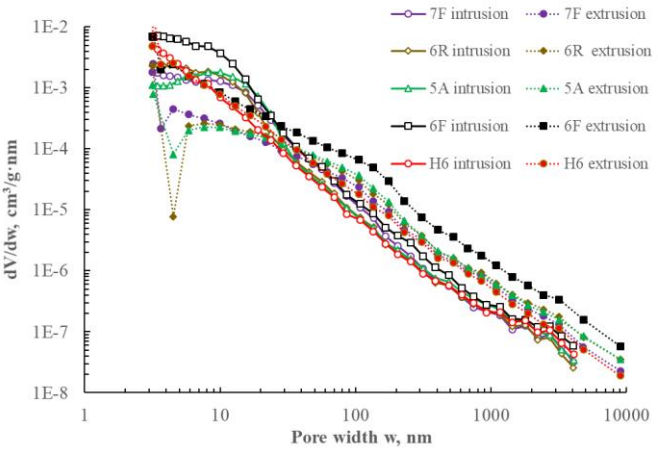

Figure 6. PSDs for the studied five samples by mercury intrusion and extrsion data.

Table 3. High pressure MIP analysis.

name	pore volume, cm^3/g	porosity %	pore SA, m^2/g	mesopore volume	mesopore SA
7F	0.0292	7.26	11.71	88.3%	98.7%
6R	0.0313	7.80	14.87	92.1%	99.3%
5A	0.0339	8.33	12.62	89.4%	99.3%
6F	0.0732	12.30	38.09	92.2%	99.6%
H6	0.0253	4.57	14.36	86.4%	99.4%

The Hg porosimetry results are shown in Table 3. 6F black shale presents the highest Hg porosity (12.3%) and SSA (38.09 m^2/g) while H6 black shale has the least Hg porosity (4.57%) and SSA (14.36 m^2/g). 7F fireclay, 6R and 5A gray shale show comparable Hg porosity and SSA with average values being 7.8% and 13.07 m^2/g. Besides, for all the studied five samples, Hg porosity and SSA are larger than N_2 porosity and SSA obtained by DFT theory. This could result from that the curshing of the pore walls due to high pressure mercury intrusion leads to opening of closed pores. The contribution of mesopores (3-50 nm) and macropores (>50 nm) to total porosity and SSA is also listed in Table 3. Compared to N_2 adsorption result, mesopores contribute even more predominantly to the total volume and SSA obtained by MIP, indicating that the possible opening of close pores due to high pressure intrusion occurs mainly in mesopore systems.

3. WATER VAPOR ADSORPTION

Water vapor adsorption isotherms on 60-80 mesh powder samples at 25°C are obtained using the static sorption method. A constant relative humidity (RH), which is equivalent to the partial pressure ratio p/p_0 of water, is created inside a desiccator using selected aqueous saturated salt solutions according to ASTM E104-02. Since RH is very sensitive to temperature, the desiccator for water vapor adsorption experiment was immersed into a water bath to maintain a constant temperature. The RH and temperature are continuously monitored through the RH/temperature meter. To remove the most residual water, the powder samples were initially oven-dried for 16 hours at standard drying temperature 110 °C for 7F fireclay, 6R and 5R shale and at 80°C for 6F and H6 organic-rich shale. After being oven-dried, the five powder samples were put inside the desiccator with desiccants to create a 0% RH for the further removal of the residual water inside shale pores. Then water vapor adsorption test was performed under designated RH environment in a stepwise manner.

Water vapor adsorption isotherms at 25°C for the studied five samples are shown in Figure 7. 7F fireclay presents the largest water adsorption (4.6 mmol/g) with 5A gray shale the least (1.9 mmol/g). 6F black shale has an intermediate capacity to water adsorption at RH<60% while increase significantly at higher RH. Compared to 6F black shale and 6R gray shale, H6 black shale presents a larger water adsorption at RH<60% but it presents a smaller water adsorption at RH>90%, possibly resulting from that the presence of montmorillonite (8.6%) and the relatively high content of illite (29.3%) in H6 balck shale provides primary sites for adsorption at low RH while a relatively low porosity causes smaller vapor condensation at high RH.

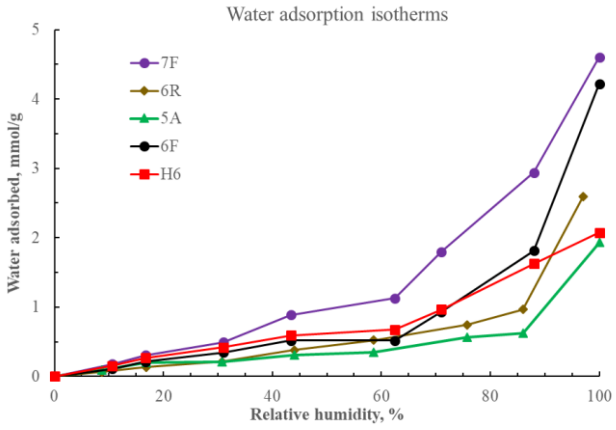

Figure 7. Water adsorption isotherms for the studied five samples based on static desiccator method.

As is shown in Figure 8, a roughly positive correlation between total water adsorption and N_2 porosity/SSA is observed. Despite the relatively low porosity, 7F fireclay has the highest total water adsorption due to its highest

SSA. The fact that 7F fireclay contains higher proportion of micropores as is shown in Figure 4 can result in intermediate porosity but high SSA. To sum up, shales with larger porosity and/or SSA tend to have a higher total water adsorption.

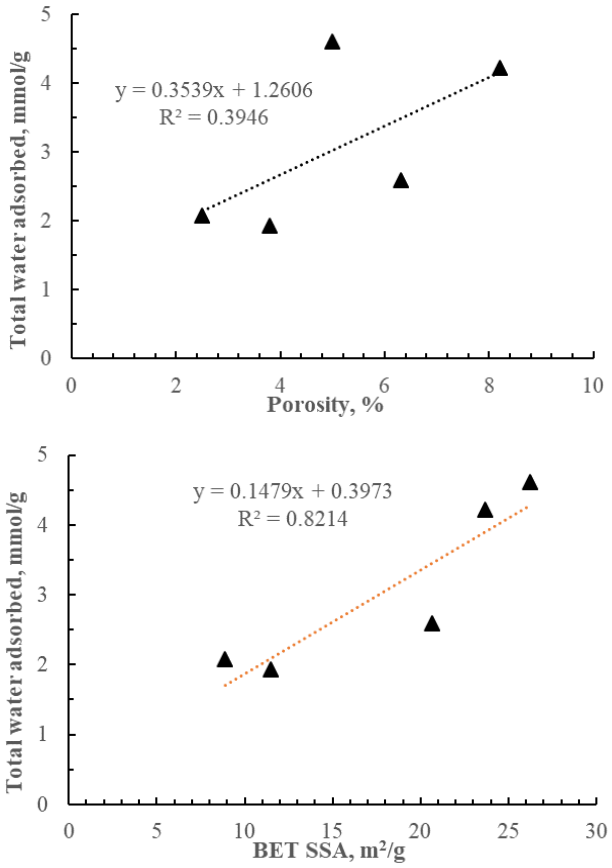

Figure 8. Correlation between N_2 porosity/SSA and total water adsorbed.

4. WATER RETENTION BEHAVIOR

The deterioration of coal mine shales associated with numerous ground control problems is highly dependent on their pore-water interactions. In general, the effect of water on shale failure can be divided in two aspects. On one hand, moisture-induced strength reduction and deterioration play an important role in shale weakening. Van Eeckhout [8] attributes moisture-induced strength reduction of rocks to several reasons, including reduction of fracture energy, pore pressurization, decrease of capillary tension, chemical deterioration, and frictional decrease. These physical/chemical effects can result in the decrease of frictional angle and/or coherence force and make the failure envelope shift down based on the Mohr-Coulomb failure criterion. On the other hand, changes in state of stress due to water uptake and/or clay swelling may also affect the stability of roof shales. Therefore, the study of shale water retention behavior plays an important role in understanding of the pore-water interaction as well as water-induced strength reduction.

The capillary potential, also called as matric suction, is one of the main causes of water retention in shale matrix containing a large amount of nanoscale pores. Water retention curve for the studied five samples, defined as the evolution of matric suction ψ_m with degree of saturation or water content, is closely related to their pore size distributions. Assume the porosities of the studied five samples maintain constant, which maybe not realistic but reasonably acceptable to evaluate their water retention characteristics. Changes in void volume due to water-induced clay swelling and variations of osmotic suction with respect to water content are not considered in this study. Water retension curve of the studied five samples could be expressed as variations in matric suction with respect to the degree of saturation. According to the well-known Laplace equation, the relation between matric suction ψ_m and pore radius r could be expressed as

$$\psi_m = \frac{2\gamma \cos\theta}{r} \quad (1)$$

where γ is interfacial tension between air and water; θ is contact angle between water interface and the shale matrix surface.

The saturation degree of the studied five samples, defined as volume of filled pores up to a given radius r divided by total pore volume V_t, could be expressed as,

$$S = \frac{1}{V_t}\int_{r_{min}}^{r} \frac{dV}{dr} dr \quad (2)$$

where dV/dr is the differential distribution of pore volume over a large range of pore size from ~1.5 nm to tens of microns, obtained by the combination of N_2 adsorption and mercury porosimetry analysis in the former section.

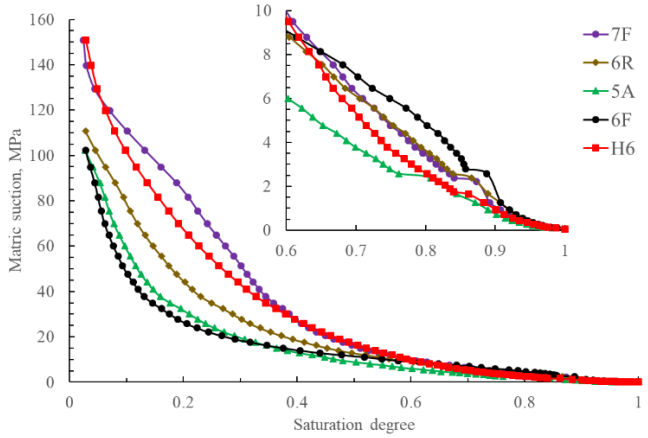

Figure 9. Water retention characteristics based on the PSDs of the studied five samples.

Figure 9 describes the shale water retention characteristics for the studied five samples. Matric suctions for the studied five samples come to ~100-150 MPa at degree of saturation equals ~ 3%, which are much higher than that of sandstones and also higher than matric suction of Tournemire shale (France) in the literature [9]. According to the Laplace equation (Eq.1), micro/meso-

pores correspond to suctions up to ~100 MPa or even more. Therefore, a large proportion of micro/meso-pores in the studied five samples lead to a very strong water holding capacity. Additionally, suctions in the studied five samples remain fairly high values (~2-5 MPa) at degree of saturation ~80%.

Among all the samples, 7F fireclay presents the largest matric suction at $S< 0.4$ and remains relatively large value at $S>0.4$, suggesting an overall strong water retention capacity. 6F black shale presents a relatively low suction at $S<0.6$ but relatively high suction at $S>0.6$. Compared to 6F black shale and 6R gray shale, H6 black shale presents a higher suction at $S<0.6$ while a lower suction at $S>0.6$. 5A gray shale behaves a relatively lower suction than other samples over the whole range of saturation degree. This trend is well consistent with the amount of water adsorbed under different RH shown in Figure 7. Instinctively, suction corresponds to water retention capacity while total porosity/SSA corresponds to total amount of water adsorbed. However, the combination of water adsorption isotherms (Figure 7) and water retention curves (Figure 9) indicates that matric suction also has a positive correlation with the amount of water adsorbed. To summarize, shales with higher proportion of smaller pores tend to have higher SSA and higher matric suction, thus leading to more water adsorption. Pore morphology of shales, therefore, plays an important role in determining water retention and adsorption behavior.

5. CONCLUSION

In this study, nanoscale pore characteristics of one fireclay and four shale sample were studied based on low pressure N_2 adsorption and MIP techniques. Water retention characteristics, based on the obtained PSDs, was also built to link nanoscale pore structure and water adsorption behavior. Several conclusions are made.

(1) Overall, Hg porosity is in good agreement with N_2 porosity for the studied five samples. Hysteresis between mercury intrusion and extrusion process can be due to structural hysteresis. Intrusion process is controlled by pore neck sizes, whereas extrusion is controlled by pore body sizes. Besides, overestimation of porosities from mercury intrusion porosimeter analysis can result from opening of closed mesopores due to high pressure.

(2) Mesopore predominantly contributes to the total pore volume for the studied fireclay and shales. Since matric suction is reversely proportional to pore size, a large proportion of mesopores lead to a strong water retention capacity.

(3) Water retention characteristics, based on pore size distribution, is closely associated to the amount of water adsorption. There is a positive correlation between porosity/SSA and total water adsorption. Besides, matric suction also shows an obviously positive correlation with the amount of water adsorbed. Under the same RH condition, higher matric suction contributes to more water uptake.

ACKNOWLEDGEMENT

This work was financially supported by The National Institute of Occupational Safety and Health (NIOSH) under the contract No. NIOSH-200-2016-90385.

REFERENCES

1 Bajpayee T, Pappas DM, Ellenberger JL. Roof Instability: What Reportable Noninjury Roof Falls in Underground Coal Mines Can Tell Us. Professional Safety 2014;59:57.

2 Molinda GM. Geologic hazards and roof stability in coal mines 2003.

3 Esterhuizen G, Bajpayee T, others. Horizontal stress related failure in bedded mine roofs-insight from field observations and numerical models. 46th US Rock Mechanics/Geomechanics Symposium, American Rock Mechanics Association; 2012.

4 Iannacchione A, Esterhuizen G, Bajpayee T, Swanson P, Chapman M, others. Characteristics of mining-induced seismicity associated with roof falls and roof caving events. Alaska Rocks 2005, The 40th US Symposium on Rock Mechanics (USRMS), American Rock Mechanics Association; 2005.

5 Murphy M. Shale Failure Mechanics and Intervention Measures in Underground Coal Mines: Results From 50 Years of Ground Control Safety Research. Rock Mechanics and Rock Engineering 2016;49:661–671.

6 Van Eeckhout EM, Peng SS. The effect of humidity on the compliances of coal mine shales. International Journal of Rock Mechanics and Mining Sciences & Geomechanics Abstracts, vol. 12, Elsevier; 1975, p. 335–340.

7 Aughenbaugh N, Bruzewski R. Humidity effects on coal mine roof stability. Contract H0232057, University of Missouri—Rolla, USBM OFR 1976:5–78.

8 Van Eeckhout EM. The mechanisms of strength reduction due to moisture in coal mine shales. International Journal of Rock Mechanics and Mining Sciences & Geomechanics Abstracts, vol. 13, Elsevier; 1976, p. 61–67.

9 Schmitt L, Forsans T, Santarelli F. Shale testing and capillary phenomena. International journal of rock mechanics and mining sciences & geomechanics abstracts, vol. 31, Elsevier; 1994, p. 411–427.

10 Yang Y, Zhou J, Xu F, Xing H. An Experimental Study on the Water-Induced Strength Reduction in Zigong Argillaceous Siltstone with Different Degree of Weathering. Advances in Materials Science and Engineering 2016;2016.

11 Zhao Y, Xue S, Han S, Chen Z, Liu S, Elsworth D, et al. Effects of microstructure on water imbibition in sandstones using X-ray computed tomography and neutron radiography. Journal of Geophysical Research: Solid Earth 2017;122:4963–4981.

12 Zhao J, Jin Z, Hu Q, Jin Z, Barber TJ, Zhang Y, et al. Integrating SANS and fluid-invasion methods to characterize pore structure of typical American shale oil reservoirs. Scientific Reports 2017;7:15413.

13 Al Ismail MI, Zoback MD. Effects of rock mineralogy and pore structure on stress-dependent permeability of shale samples. Phil Trans R Soc A 2016;374:20150428.

[14] Sang G, Elsworth D, Miao X, Mao X, Wang J. Numerical study of a stress dependent triple porosity model for shale gas reservoirs accommodating gas diffusion in kerogen. Journal of Natural Gas Science and Engineering 2016;32:423–438.

15 Ju Y, Yang Y, Peng R, Mao L. Effects of pore structures on static mechanical properties of sandstone. Journal of Geotechnical and Geoenvironmental Engineering 2013;139:1745–1755.

16 Lin B, Chen M, Jin Y, Pang H. Modeling pore size distribution of southern Sichuan shale gas reservoirs. Journal of Natural Gas Science and Engineering 2015;26:883–894.

17 Hall C, Hoff WD. Water transport in brick, stone and concrete. CRC Press; 2011.

18 Hatzor Y, Palchik V. The influence of grain size and porosity on crack initiation stress and critical flaw length in dolomites. International Journal of Rock Mechanics and Mining Sciences 1997;34:805–816.

19 Javadpour F, Moravvej Farshi M, Amrein M, others. Atomic-force microscopy: a new tool for gas-shale characterization. Journal of Canadian Petroleum Technology 2012;51:236–243.

20 Chalmers GR, Bustin RM, Power IM. Characterization of gas shale pore systems by porosimetry, pycnometry, surface area, and field emission scanning electron microscopy/transmission electron microscopy image analyses: Examples from the Barnett, Woodford, Haynesville, Marcellus, and Doig units. AAPG Bulletin 2012;96:1099–1119.

21 Dieterich M, Kutchko B, Goodman A. Characterization of Marcellus Shale and Huntersville Chert before and after exposure to hydraulic fracturing fluid via feature relocation using field-emission scanning electron microscopy. Fuel 2016;182:227–235.

22 Wang Y, Zhu Y, Chen S, Li W. Characteristics of the nanoscale pore structure in Northwestern Hunan shale gas reservoirs using field emission scanning electron microscopy, high-pressure mercury intrusion, and gas adsorption. Energy & Fuels 2014;28:945–955.

23 Kuila U, Prasad M. Specific surface area and pore-size distribution in clays and shales. Geophysical Prospecting 2013;61:341–362.

24 Bahadur J, Melnichenko Y, Mastalerz M, Furmann A, Clarkson CR. Hierarchical pore morphology of cretaceous shale: a small-angle neutron scattering and ultrasmall-angle neutron scattering study. Energy & Fuels 2014;28:6336–6344.

25 Mastalerz M, He L, Melnichenko YB, Rupp JA. Porosity of coal and shale: Insights from gas adsorption and SANS/USANS techniques. Energy & Fuels 2012;26:5109–5120.

26 Bahadur J, Radlinski AP, Melnichenko YB, Mastalerz M, Schimmelmann A. Small-angle and ultrasmall-angle neutron scattering (SANS/USANS) study of New Albany Shale: a treatise on microporosity. Energy & Fuels 2015;29:567–576.

27 Aylmore L, Quirk J. The micropore size distributions of clay mineral systems. European Journal of Soil Science 1967;18:1–17.

28 Clarkson CR, Solano N, Bustin R, Bustin A, Chalmers G, He L, et al. Pore structure characterization of North American shale gas reservoirs using USANS/SANS, gas adsorption, and mercury intrusion. Fuel 2013;103:606–616.

29 Gregg S, Sing K. Adsorption, Surface Area and Porosity (Academic, New York, 1982). Google Scholar n.d.:46.

30 Quirk J, Aylmore L. Domains and quasi-crystalline regions in clay systems. Soil Science Society of America Journal 1971;35:652–654.

31 Groen JC, Peffer LA, Pérez-Ramírez J. Pore size determination in modified micro-and mesoporous materials. Pitfalls and limitations in gas adsorption data analysis. Microporous and Mesoporous Materials 2003;60:1–17.

32 Washburn EW. Note on a method of determining the distribution of pore sizes in a porous material. Proceedings of the National Academy of Sciences 1921;7:115–116.

33 Giesche H. Mercury porosimetry: a general (practical) overview. Particle & Particle Systems Characterization 2006;23:9–19.

34 Lowell S. Continuous scan mercury porosimetry and the pore potential as a factor in porosimetry hysteresis. Powder Technology 1980;25:37–43.

35 Lowell S, Shields JE. Theory of mercury porosimetry hysteresis. Powder Technology 1984;38:121–124.

36 Conner Jr WC, Lane A, Hoffman A. Measurement of the morphology of high surface area solids: hysteresis in mercury porosimetry. Journal of Colloid and Interface Science 1984;100:185–193.

37 Wardlaw NC, McKellar M, Yu L. Pore and throat size distributions determined by mercury porosimetry and by direct observation. Carbonates and Evaporites 1988;3:1.

38 Conner W, Cevallos-Candau J, Weist E, Pajares J, Mendioroz S, Cortes A. Characterization of pore structure: porosimetry and sorption. Langmuir 1986;2:151–154.